




Cite this: DOI: 10.1039/d5lp00243e

Information encryption gels based respectively on acid-induced response and fluorescence resonance energy transfer white-light materials

Tingting Zhang, Juan Zhang, Yanyan Li, Caiyuan Guo, Yuehua Liang, Jiuzhi Wei, Xinxian Ma * and Xinning Han*

In this study we developed white light-emitting gel materials based on two mechanisms, namely, acid-induced protonation and Förster resonance energy transfer (FRET), and applied them to information protection and encryption. The newly synthesized compound, **Q**, forms different protonation states after protonation, and the multicolor emissions from these states ultimately achieve white-light emission through spectral superposition. When **Q** is paired with dyes such as Nile red, rhodamine 6G, and acridine red, it can act as an energy donor in the FRET system, enabling white-light emission at a specific, optimized ratio. Two functional gels based on polyvinyl alcohol (PVA) were developed, namely a PVA–Q–Nile red composite material and a PVA–Q–H⁺ (150 eq. H⁺ to **Q**) responsive gel. These gels exhibit stable white light emission properties and can be used for writing and encrypting high-resolution information. Additionally, the PVA–Q–H⁺ responsive gel possesses time-dependent encryption functionality: triggered by OH[−], the written traces can realize controllable self-erasure. The gel material developed in this study based on a white-light emission system with dual-responsive mechanisms provides a novel strategy for the design and synthesis of intelligent anti-counterfeiting materials.

Received 1st August 2025,
Accepted 5th October 2025

DOI: 10.1039/d5lp00243e

rsc.li/rscappliedpolym

1. Introduction

Information encryption and anti-counterfeiting technology play a crucial role in various fields of contemporary society.^{1,2} Against this backdrop, the development of novel fluorescent materials with dynamic response characteristics is not only of great significance for basic research but also provides inspiration and possibilities for the design of next-generation advanced anti-counterfeiting inks.^{3,4} Among these materials, white light-emitting (WLE) materials have attracted extensive attention due to their complex emission spectra and richer dimensions of chromatic information, which enable higher-capacity and higher-level encryption.^{5,6}

At present, the main strategies for constructing WLE materials include single-molecule systems,⁷ supramolecular assemblies,^{8,9} metal–organic frameworks,¹⁰ and energy transfer mechanisms based on fluorescence resonance energy transfer (FRET).¹¹ These strategies have been successfully applied to the preparation of WLE gels. Notably, gel materials, due to their high tunability, provide flexibility for customized information encryption and have been widely applied in anti-

counterfeiting fields such as food safety and 3D anti-counterfeiting printing.^{12–15} Although gels with excellent stability can be prepared based on single-molecule white-light emission systems,¹⁶ these systems pose significant challenges in molecular design.¹⁷ For instance, Liang *et al.*¹⁸ designed a single-molecule WLE hydrogel through dual acid–base channel regulation, enabling time-dependent and water vapor-responsive information encryption; Wang *et al.*¹⁹ developed a thermo-responsive hydrogel that achieved dynamic WLE by regulating the protonation equilibrium of fluorophores *via* temperature control. However, such regulation mechanisms relying on a single external stimulus have inherent limitations: their emission colors are indirectly adjusted by altering the microenvironment of the polymer, and combined with the thermal hysteresis characteristics of hydrogels, it is difficult to maintain the WLE state accurately and stably.

Beyond single-molecule systems, FRET is also a critical mechanism for achieving WLE. This provides another important pathway for realizing efficient and tunable WLE. Its effective operation requires the fulfillment of three core conditions: (i) the donor–acceptor distance is maintained within the range of 1–10 nanometers; (ii) the emission spectrum of the donor sufficiently overlaps with the absorption spectrum of the acceptor; and (iii) the spatial arrangement of donor–acceptor transition dipoles is appropriate.^{20–23} FRET assisted white-light emission serves as a remarkably concise and advanced function

Ningxia Key Laboratory of Green Catalytic Materials and Technology, College of Chemistry and Chemical Engineering, Ningxia Normal University, Guyuan 756099, China. E-mail: maxinxian@163.com

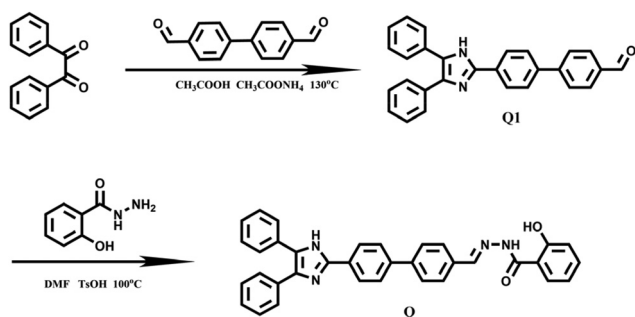


in high-level anti-counterfeiting.²⁴ For example, Ma *et al.*²⁵ developed a WLE hydrogel with both information protection writing and alkaline gas detection capabilities; Mardani *et al.*²⁶ regulated white-light emission WLE by adjusting the efficiency of FRET through temperature and pH, and this approach has been widely applied. This provides insights for the design of multi-responsive information encryption materials.

Based on the above research, it has been observed that most current organic WLE systems either rely on a single modulation mechanism or suffer from complexity and uncontrollability caused by the introduction of multi-mechanism coupling. Therefore, significant challenges are faced in meeting the comprehensive requirements for the flexibility and precision of luminescence regulation in the field of information encryption, which makes the development of novel multiple pathways and mechanism regulation systems an urgent need. To address the aforementioned issues, this study innovatively proposes a dual-responsive WLE system. Its core advantage lies in providing two parallel and completely independent regulation channels for achieving stable and reversible white-light emission: the first is an acid-induced intra-

molecular protonation channel, and the second is an intermolecular FRET energy transfer channel. Compared with existing systems, this design not only overcomes the dependence on a single external stimulus, but also avoids the complexity and uncontrollability caused by multi-mechanism coupling, thereby significantly improving the regulation precision and operational flexibility of white-light emission.

Specifically, a new fluorescent compound, **Q** (Scheme 1), was designed and synthesized, and its luminescence properties were verified with time-dependent density functional theory (TD-DFT) calculations. This molecule can generate white light either through acid-induced intramolecular protonation or through intermolecular FRET processes with acridine red, rhodamine 6G (Rh6G), and Nile red. Furthermore, two multifunctional gels, PVA-**Q**-Nile red and PVA-**Q**-H⁺ (150 eq. H⁺ to **Q**), were prepared using polyvinyl alcohol (PVA) as the matrix. Both gels are capable of information writing and encryption. Among them, the time-varying properties of the PVA-**Q**-H⁺ gel enable automatic information erasure through the action of OH⁻, effectively preventing the risk of secondary leakage and providing a new direction for the research and development of information encryption materials (Fig. 1).



Scheme 1 Synthesis of **Q1** and **Q**.

2. Experimental

2.1 Materials and general methods

PVA (polymerization degree = 1799, 98–99% alcoholysis) was purchased from Energy Chemical. Benzil, 4,4'-biphenyldicarboxaldehyde, acetic acid, ammonium acetate, salicyl hydrazide, ethanol, *p*-methylbenzene sulfonic acid (*p*-TsOH), *N,N*-dimethylformamide (DMF), dimethyl sulfoxide (DMSO), Rh6G, acridine red, Nile red, ammonium hydroxide, sulfuric acid, and sodium hydroxide were purchased from Sinopharm

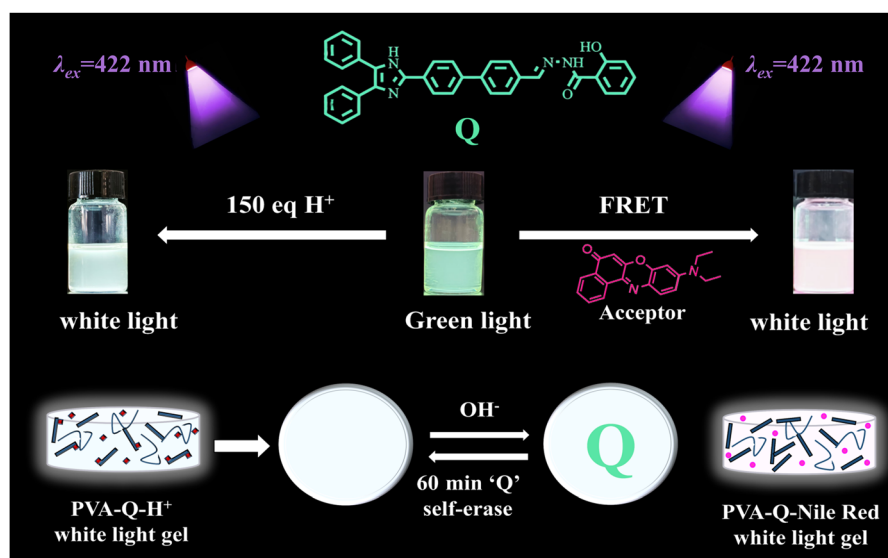


Fig. 1 Schematic diagram of white light emission regulated by acid-induced protonation ($\lambda_{em} = 518$ nm) and FRET dual mechanisms under $\lambda_{ex} = 422$ nm, along with its application in information encryption.



Chemical Reagent Co., Ltd. All the compounds were used directly without further purification, and distilled water was used for all experiments.

Proton nuclear magnetic resonance (^1H NMR; 400 MHz) and ^{13}C NMR (101 MHz) spectroscopic analyses were performed using a 400 MHz Bruker spectrometer. A Shimadzu RF-6000 fluorescence spectrophotometer was used to obtain the fluorescence spectra. Mass spectrometry was performed using an Autoflex Speed TOF/TOF. Fourier transform infrared (FT-IR) spectra of the samples were obtained using an IR spectro-photometer (Thermo Scientific Nicolet iS5) in a wavenumber range of 400–4000 cm^{-1} . The quantum yields (QYs) were determined using an Edinburgh FLS1000 instrument. A Shimadzu UV-1750 spectrometer was used to record the ultraviolet-visible (UV-vis) absorption spectra of the samples. The fluorescence lifetimes were recorded with a time-correlated single-photon counting spectrometer (Edinburgh FLS1000). Quantum chemistry calculations were performed at the PBE0/6-311G* level of theory based on TD-DFT using Gaussian 09 software.

2.2 Synthesis of compound Q1

As shown in Scheme 1, a mixture of benzil (4.00 g, 19.03 mmol), 4,4'-biphenyldicarboxaldehyde (4.00 g, 19.03 mmol), and ammonium acetate (7.33 g, 95.15 mmol) in acetic acid (60 mL) was stirred at 130 °C for 6 h. After cooling to room temperature, the reaction mixture was poured into ice-water (400 mL), and the pH value was adjusted to neutral using aqueous ammonia. The resulting precipitate was collected using suction filtration and washed thoroughly with cold water (3×400 mL). The solid was dried under vacuum yielding the product as a yellow powder (6.77 g, 84.6% yield). ^1H NMR (400 MHz, $\text{DMSO}-d_6$, Fig. S1) δ 12.81 (d, $J = 17.0$ Hz, 1H), 10.08 (d, $J = 6.8$ Hz, 1H), 8.22 (t, $J = 8.3$ Hz, 2H), 8.03 (d, $J = 6.2$ Hz, 4H), 7.92 (t, $J = 8.1$ Hz, 2H), 7.55 (dd, $J = 17.0$, 7.5 Hz, 4H), 7.47 (t, $J = 7.5$ Hz, 2H), 7.39 (t, $J = 7.3$ Hz, 1H), 7.32 (t, $J = 7.6$ Hz, 2H), 7.24 (t, $J = 7.3$ Hz, 1H).

2.3 Synthesis of compound Q

As shown in Scheme 1, a mixture of compound Q1 (2.00 g, 5.00 mmol), salicyl hydrazide (0.76 g, 5.00 mmol), and *p*-TsOH (0.02 g, 0.12 mmol) in DMF (20 mL) was stirred at 100 °C for 10 h. After cooling to room temperature, the reaction mixture was poured into ice-water (400 mL). The resulting precipitate was collected using suction filtration and washed thoroughly with cold water (3×400 mL). The crude product was further purified by recrystallization from ethanol yielding compound Q as a yellow solid (1.53 g, 55% yield). ^1H NMR (400 MHz, $\text{DMSO}-d_6$, Fig. S2) δ 12.99 (s, 1H), 11.91 (s, 1H), 11.86 (d, $J = 2.6$ Hz, 1H), 8.52 (s, 1H), 8.22 (d, $J = 8.2$ Hz, 2H), 7.95–7.86 (m, 7H), 7.59–7.53 (m, 4H), 7.48–7.31 (m, 7H), 7.01–6.96 (m, 2H). ^{13}C NMR (101 MHz, $\text{DMSO}-d_6$, Fig. S3) δ 165.22, 159.45, 148.66, 148.58, 145.55, 145.48, 141.42, 141.26, 139.54, 139.37, 134.33, 134.12, 133.86, 129.80, 129.51, 129.11, 128.96, 128.57, 128.39, 128.38, 128.32, 127.83, 127.57, 127.44, 127.40, 127.27, 126.35, 125.98, 119.48, 117.76, 116.46. EI-MS (Fig. S4) m/z : $[\text{M} + \text{H}]^+$ calcd: 535.38. Found: 535.21.

2.4 Synthesis of PVA-Q-Nile red gel

PVA (2.2 g, 0.05 mol, alcoholysis degree 499.5 mol%) was dissolved in 10 mL of DMSO solution with Q and Nile red in a ratio of 50 : 1 ($[\text{Q}] = 1 \times 10^{-3}$ mol L^{-1}). The mixture was heated and stirred at 100 °C for 6 h, then poured into a Petri dish and refrigerated at -10°C for 12 h. After taking it out and thawing, a white fluorescent PVA-Q-Nile red gel was obtained.

2.5 Synthesis of PVA-Q-H⁺ gel

PVA (2.2 g, 0.05 mol, alcohol degree >99.5 mol%) was dissolved in 10 mL of DMSO solution with sulfuric acid and Q in a ratio of 150 : 1 ($[\text{Q}] = 1 \times 10^{-3}$ mol L^{-1}). The mixture was heated and stirred at 100 °C for 6 h, then poured into a Petri dish and refrigerated at -10°C for 12 h. After taking it out and thawing, a white fluorescent PVA-Q-H⁺ gel was obtained.

3. Results and discussion

3.1 Theoretical calculation

After establishing the synthetic route for molecule Q, TD-DFT calculations were performed to evaluate its fluorescence properties and synthetic potential.²⁷ As dimethyl sulfoxide (DMSO) was determined to be the optimal solvent for Q, DMSO was employed as the solvent system in all subsequent experiments. Linear response theory was used for computational modeling, with the DMSO environment represented using the polarizable continuum model.

First, the geometric configuration of the solvated system was optimized using the hybrid functional PBE0/6-311G* basis set. Subsequently, by optimizing the first singlet excited state (S_1) structure of Q in DMSO, we obtained the $S_0 \rightarrow S_1$ excitation energy and corresponding molecular orbital diagrams (Fig. 2a). The fluorescence emission spectrum was then simulated using the Multiwfn program, yielding a calculated emission wavelength of 512 nm for Q.²⁸ Experimentally, the emission maximum of Q in DMSO solution was measured at 522 nm (Fig. 2b), demonstrating excellent consistency with the theoretical prediction. Furthermore, the excitation and emission spectra of Q were experimentally recorded (Fig. 2c), with follow-up measurements performed using a fixed excitation wavelength of 422 nm for photophysical characterization.

3.2 Aggregation-caused quenching (ACQ) effect

During experimental characterization, compound Q was found to exhibit typical ACQ behavior. Since substance Q is almost insoluble in water, when water was gradually introduced into Q's DMSO solution (volume fraction of water: 0–90%), a systematic decrease in fluorescence intensity was observed (Fig. 3a and S5). This phenomenon is caused by the increased water content, which leads to a stronger molecular aggregation. Comparative analysis further revealed that solid-state Q samples exhibited lower fluorescence intensity under ultraviolet (UV) illumination than their DMSO solutions (Fig. 3b–e). Scanning electron microscopy characterization (Fig. S6) demonstrated well-ordered lamellar stacking of Q molecules in



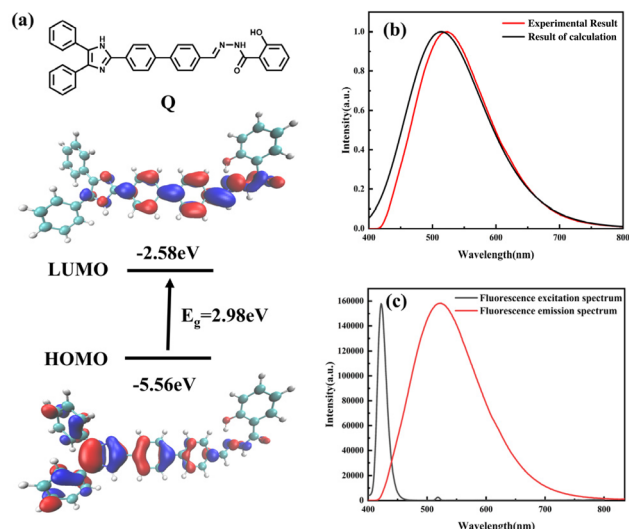


Fig. 2 (a) HOMO–LUMO energy level diagram of molecule **Q**. (b) Normalized fluorescence emission spectra from theoretical calculation (black) and experimental measurement (red). (c) Experimental excitation and emission spectra of molecule **Q**.

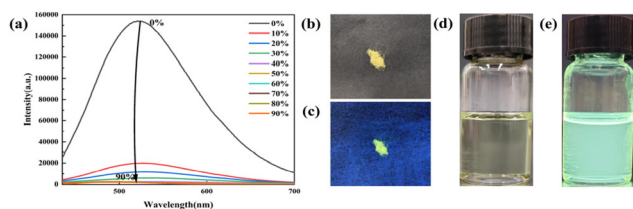


Fig. 3 (a) Fluorescence spectra of **Q** in DMSO with varying water content (0–90%). (b and d) Photographs of **Q** in solid powder and DMSO solution under ambient light. (c and e) Corresponding photographs under 422 nm UV irradiation.

the solid state. This compact arrangement facilitates increased intermolecular nonradiative energy transfer, consequently suppressing radiative decay pathways and causing the characteristic ACQ phenomenon.

3.3 Acid-coordination-induced white-light emission

Ion recognition tests revealed that acidic and alkaline environments differentially affect the fluorescence emission of **Q** (Fig. S7). The fluorescence quenching observed under alkaline conditions can be attributed to the deprotonation of **Q**,²⁹ generating non-emissive anionic species (Fig. S8). As revealed by NMR titration (Fig. S9 and 10), with the gradual addition of OH^- , the proton signals of the O–H, N–H1, and N–H2 groups in the original substance **Q** disappear. Meanwhile, the C–H protons in other parts of the molecule shift to higher fields. This is because the deprotonation of the molecule induced by the addition of OH^- increases the intramolecular negative charge density, leading to a shielding effect on the C–H protons and thus their chemical shifts to higher fields.

Notably, protonation of **Q** in DMSO solution induced white-light emission when the H^+ concentration reached 150 eq. (Fig. S7). To systematically investigate this acid-responsive behavior, all subsequent experiments were conducted using a DMSO solution with a constant **Q** concentration (1×10^{-3} M).

Fig. 4b and S11 show the considerable evolution of the emission spectra of **Q** in DMSO solution upon gradual addition of H^+ : the overall fluorescence intensity progressively decreased, with marked attenuation of the red (~ 620 nm) and green (~ 550 nm) emission components, while the blue component (~ 450 nm) exhibited relative enhancement. When the H^+ concentration reached 150 eq., the system achieved white-light emission. Fig. 4a, c, e and f show the systematic color changes of the fluorescent solution with an increase of H^+ concentration (0–150 eq.): initial green (0 eq.) \rightarrow yellow-green (5 eq.) \rightarrow yellow-white (60 eq.) \rightarrow white light (150 eq.). At 150 eq. H^+ , the CIE coordinates are (0.29, 0.33), which is very close to the pure white light emission with chromaticity coordinates (0.33, 0.33) in the 1931 Commission Internationale de l'Éclairage (CIE) standard chromaticity system.³⁰ The observed phenomenon likely stems from distinct fluorescence emissions generated by different protonation states of **Q**, with spectral superposition of these multicolor emissions governing white-light generation.

To analyze the H^+ -induced structural modification, we conducted ^1H NMR (Fig. S12 and S13) spectroscopy analysis in combination with the ESP of molecule **Q** (Fig. 4d). During the gradual addition of H^+ to the $\text{DMSO}-d_6$ solution of **Q**, the nitrogen atom on the imidazole ring was found to be preferentially protonated. After protonation, the electron cloud density of the imidazole ring system decreased significantly, resulting in a strong deshielding effect. This deshielding effect caused the proton peak of N–H on the imidazole ring and the proton peak of C–H ($\delta = 8.2$ ppm) on the adjacent benzene ring to shift to the low field. With the continuous addition of H^+ , the C=N bond in the hydrazone structure underwent protonation. Similarly, due to the deshielding effect, the signal peak of C–H at 7.9 ppm on the adjacent benzene ring also shifted to the low field. The absence of a significant change in the C–H signal peak at 7.0 ppm indicated that the –OH group was not protonated. The signal peaks of N–H and –OH in the hydrazone structure weakened or even disappeared because the acidic environment accelerated the proton exchange rate. The shift of the C–H signal peak at 7.3–7.5 ppm to the low field might be attributed to the protonation of **Q**, which reduced the electron cloud density and electronegativity while enhancing the deshielding effect, thereby causing rotation of some structures in the molecule. The structure of molecule **Q** after protonation is shown in Fig. S14. This redistribution of electrons modulates the π -conjugated system, ultimately affecting the luminescence properties. When the concentration of H^+ reached 150 eq., almost all free **Q** molecules in the solution were converted into substances in different protonation states. The luminescence superposition effect of these different protonated forms is the fundamental reason for the generation of white-light emission.



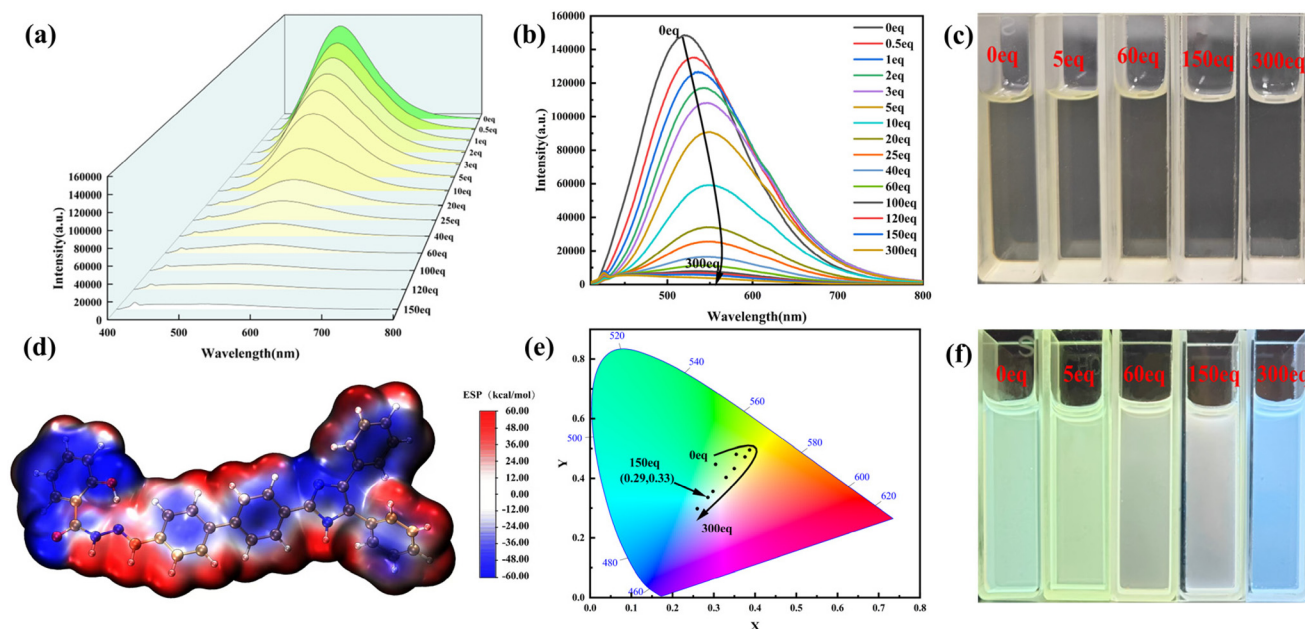


Fig. 4 (a) Fluorescence color evolution of **Q** in DMSO solution with varying H^+ equivalent concentrations. (b) Emission spectra of **Q** (1×10^{-3} M in DMSO) as a function of H^+ concentration (0–300 eq.). (c) Visible-light photographs showing the color progression of **Q** in DMSO with increasing H^+ content. (d) Simulated electrostatic potential (ESP) distribution of **Q**. (e) Corresponding CIE chromaticity diagram for (b). (f) Corresponding UV-illuminated (422 nm) photographs demonstrating the fluorescence color transition for (c).

Subsequently, UV-vis spectroscopy (Fig. S15) was employed to analyze the protonation process of **Q** in DMSO. Consistent with the NMR observations, a distinct hypsochromic shift of 10 nm (from 361 to 351 nm) in the characteristic absorption peaks was observed during progressive protonation, with the spectra showing no further changes upon reaching the saturated protonation state.

Finally, FT-IR spectroscopy (Fig. S16) confirmed the interaction between **Q** and H^+ after the addition of 150 eq. H^+ . The carbonyl stretching vibration of pristine **Q** at 1648 cm^{-1} exhibited a bathochromic shift to 1633 cm^{-1} upon protonation, providing direct evidence of $Q-H^+$ interactions.

3.4 White light emission achieved by FRET

The absorption spectra of RhB, acridine red, Rh6G, nuclear fast red, and Nile red were collected and compared with the emission spectrum of **Q** in DMSO solution (1×10^{-3} M) (Fig. 5a). To determine whether these dyes could undergo FRET with **Q**, further experiments were conducted. The results demonstrated that only Rh6G, acridine red, and Nile red were capable of engaging in FRET with **Q**. Fig. 5b and S17 present the CIE chromaticity diagram and white-light emission spectra of **Q** mixed with Rh6G, acridine red, and Nile red at optimized ratios, confirming successful white-light emission. After evaluating spectral overlap, emission intensity, white-light purity, and energy transfer efficiency (Table S1), we primarily focused on the **Q**-Nile red system, while the corresponding data for **Q**-acridine red and **Q**-Rh6G are provided in the SI (Fig. S18 and 19).

As shown in Fig. 5a, **Q** in DMSO exhibits a strong fluorescence emission peak at 522 nm, with an emission band

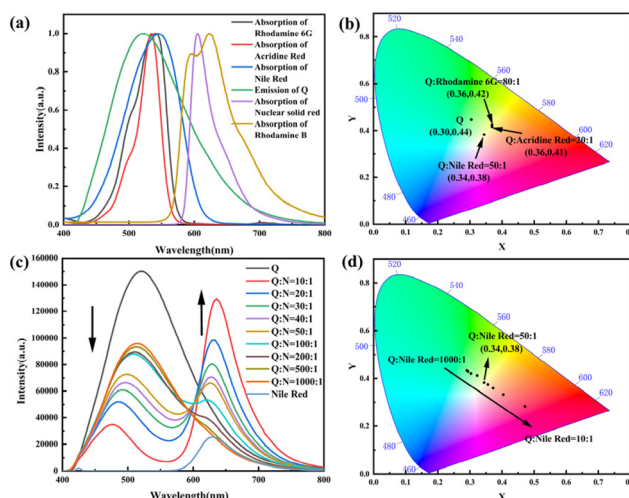


Fig. 5 (a) Normalized emission spectrum of **Q** and normalized absorption spectra of five fluorescent dyes. (b) CIE chromaticity diagram of white light emission from **Q** mixed with acridine red, Nile red, and Rh6G at molar ratios of 20 : 1, 50 : 1, and 80 : 1, respectively. (c) Fluorescence emission spectra of **Q** with Nile red in DMSO at different molar ratios. (d) Corresponding CIE chromaticity diagram for (c).

spanning 400–750 nm. In contrast, Nile red in DMSO displays a maximum absorption peak at 545 nm, covering an absorption range of 400–640 nm, demonstrating the best spectral overlap with **Q**'s emission. Although the **Q**-Nile red system exhibits relatively weak overall emission intensity (Table S1), white-light emission is achieved at a molar ratio of 50 : 1 (Nile

red:Q) under 422 nm excitation, with CIE coordinates of (0.34, 0.38), closely approaching the pure white-light reference point (0.33, 0.33). As shown in Fig. 5c, upon excitation at 422 nm, gradual addition of Nile red to a 1×10^{-3} M solution of Q in DMSO resulted in a systematic decrease in the fluorescence intensity of Q at 522 nm, accompanied by the emergence of a new emission band at 630 nm. Concurrently, the fluorescence intensity of Nile red progressively increased, reaching its maximum at a Q-to-Nile red molar ratio of 10:1. Comparative analysis of the fluorescence emission profiles between the Q-Nile red system (10:1 molar ratio) and pure Nile red confirmed the occurrence of FRET. Notably, under 422 nm excitation, pure Nile red exhibited weak fluorescence intensity, and increasing its concentration did not enhance emission. The observed intensity increase at 630 nm is attributed to efficient energy transfer from Q to Nile red. The fluorescence quantum yield of the Q-Nile red system and pure Q were 40.1% and 58.1%, (Fig. S21). Subsequently, the fluorescence decay experiment showed that the lifetimes decreased from the Q ($\tau = 2.29$ ns) system to the Q-Nile red system ($\tau = 2.16$ ns) (Fig. S20), indicating that the energy harvested by Q had been successfully transferred to Nile red.

3.5 Gel-based writing materials for information encryption

Building upon these findings, we incorporated Q into polymeric gels using PVA as the carrier and developed two novel information encryption systems, namely PVA-Q-Nile red gel and PVA-Q- H^+ gel. Firstly, we dissolved PVA in a DMSO solution (Fig. S22), then added Q and Nile red at a mass ratio of 50:1 (Q:Nile red). The resulting mixture was heated and stirred at 100 °C for 6 hours, after which it was poured into a Petri dish and refrigerated at -10 °C for 12 hours. After removal and thawing, the PVA-Q-Nile red gel with white fluorescence was obtained. The chromaticity coordinates of its white light emission were (0.32, 0.34) (Fig. S17a), which were closer to the ideal white point (0.33, 0.33) compared with the DMSO solution of Q and Nile red. This phenomenon is presumably attributed to the selective absorption of red light in the system by the PVA gel matrix. Considering that Q can emit green fluorescence with low intensity in the presence of an alkali, we used an aqueous OH^- solution to write on the as-prepared gel (Fig. S23). No obvious writing traces were observed on the gel under natural light; however, distinct writing traces became visible under a 442 nm UV lamp. Owing to this unique property, the PVA-Q-Nile red gel can serve as a

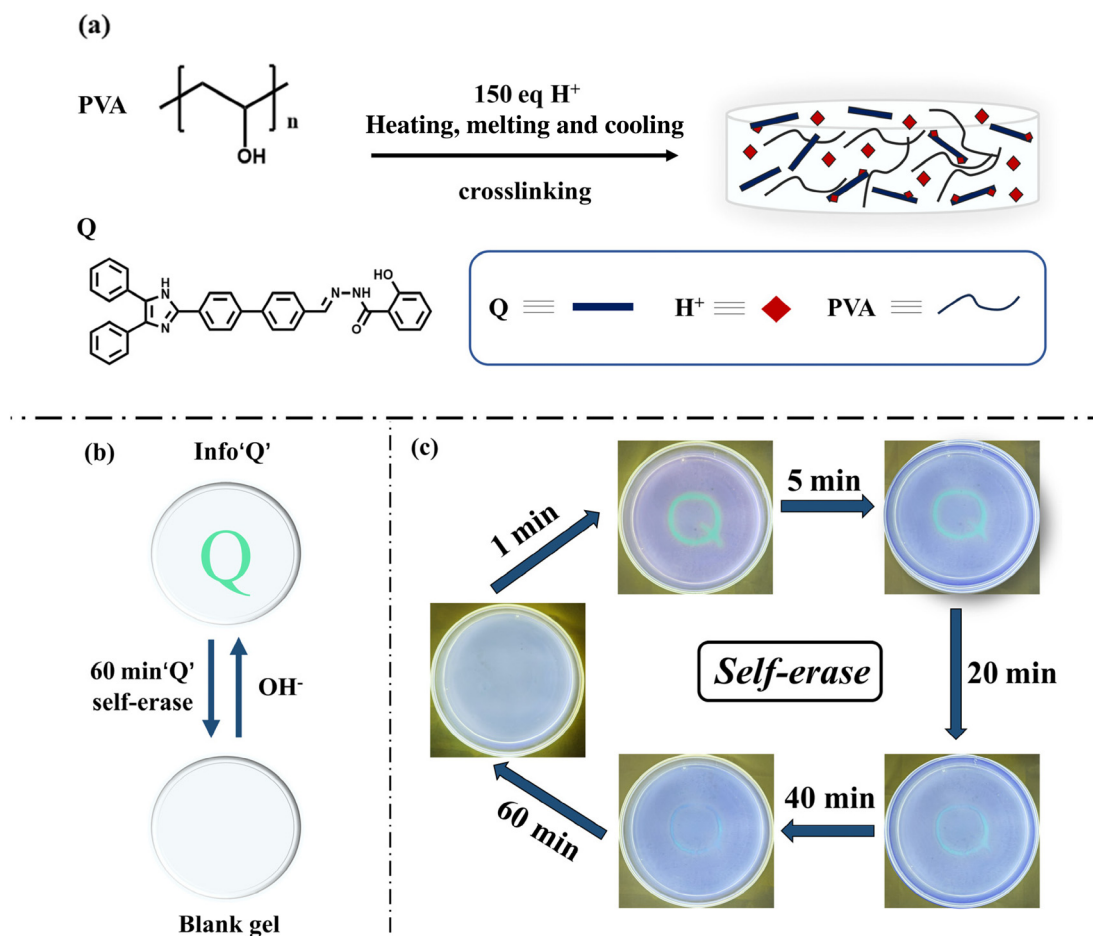


Fig. 6 (a) Schematic showing the fabrication process of the PVA-Q- H^+ gel. (b) Schematic of information-encoding and self-erasing process of the PVA-Q- H^+ gel. (c) Photograph of PVA-Q- H^+ gel self-erasing process with time under UV light.



dedicated writing material to realize the protection and encryption of information.

Subsequently, using the same matrix preparation method, we further synthesized the PVA-Q-H⁺ white fluorescent gel (Fig. 6a). Intermolecular hydrogen bonds may have been formed between PVA and molecule **Q** through cross-linking interactions (Fig. S24).³¹ These hydrogen bond interactions can effectively restrict the free movement of **Q** molecules but do not affect the migration of H⁺. We used an aqueous OH[−] solution to write on the surface of the PVA-Q-H⁺ gel (Fig. 6b and c). When the gel surface came into contact with OH[−], a deprotonation reaction occurred, forming a distinct green fluorescent region. As time elapsed, the written traces showing green fluorescence gradually faded and completely disappeared after 60 minutes, with the written region reverting to the initial white fluorescence. This information “self-erasing” phenomenon is presumably due to the fact that the H⁺ concentration inside the gel is higher than that of the externally introduced OH[−]. When the OH[−] on the surface of the gel is completely consumed, since H⁺ can migrate freely within the gel, the depleted H⁺ in the system is replenished over time, causing the **Q** molecules in the writing area to be protonated again, and the fluorescence will return to white. Based on this unique time-responsive property, we have developed a white-light information encryption material with time dependence.

To evaluate the structural stability of the two gels in practical applications, we further tested the elastic moduli of the PVA-Q-H⁺ gel and the PVA-Q-Nile red gel (Fig. S25). The results showed that the PVA-Q-Nile red gel had an elastic modulus of 50 kPa, and this relatively high value indicates strong rigidity and resistance to deformation under an external force. In contrast, the PVA-Q-H⁺ gel had an elastic modulus of 5 kPa, and this lower value confers weaker rigidity but greater flexibility, allowing it to deform easily under a force while maintaining good recovery ability. To verify the influence of mechanical properties on fluorescence performance, we conducted twist deformation tests on the two gels (Fig. S26), and no obvious change in their fluorescence colors was observed, demonstrating the stability of their fluorescence performance under mechanical deformation.

4. Conclusions

In this study, we designed and synthesized a novel fluorescent molecule, **Q**, which is capable of white-light emission through two distinct mechanisms: acid-induced protonation and FRET. Experimental characterization revealed that **Q** undergoes progressive protonation, and its distinct protonation states cause it to exhibit multicolor fluorescence emissions. Spectral analysis confirmed that the additive combination of these emissions successfully generated white light. Furthermore, compound **Q** served as an energy donor and efficiently underwent FRET with energy acceptors, including acridine red, Nile red, and Rh6G. Under optimized donor-acceptor ratio conditions, white-light emission was achieved. Leveraging these photo-

physical characteristics, we engineered two functional information encryption systems using PVA matrices: a PVA-Q-Nile red gel and PVA-Q-H⁺ gel. Specifically, upon contact with OH[−], the PVA-Q-H⁺ gel instantaneously revealed the written information. Furthermore, the written traces self-erase within a preset time frame, thereby enabling time-dependent information protection. This research offers innovative concepts for the development of novel intelligent information writing and time-dependent encryption materials.

Author contributions

Tingting Zhang: conceptualisation, methodology, investigation, and writing – original draft. Caiyuan Guo and Juan Zhang: material characterization and performance tests. Yanyan Li, Yuehua Liang, Jiuzhi Wei and Xinning Han: performance of tests. Xinxian Ma: resources and funding acquisition.

Conflicts of interest

The authors declare no conflict of interest.

Data availability

The data supporting this article have been included as part of the supplementary information (SI). Supplementary information (SI): experimental details and data from the NMR, MS, UV/vis, IR, and other experimental details and data. See DOI: <https://doi.org/10.1039/d5lp00243e>.

Acknowledgements

This work was supported by the National Natural Science Foundation of China (22462030, 32360327), the Natural Science Foundation of Ningxia, China (2024AAC02050), the Science and Technology Foundation of Guyuan, China (No. 2024BGTYF01-46), the Key Laboratory of Green Catalytic Materials and Technology of Ningxia (2025SYSZD-5), and the Innovation and Entrepreneurship Training Program for College Students in Higher Education Institutions of Ningxia, China (No. 324), all of which are gratefully acknowledged.

References

- 1 Y. Li and P. Gao, *Chemosensors*, 2023, **11**, 489.
- 2 X. Lan, S. Xu, C. Sun, Y. Zheng, B. Wang, G. Shan, Y. Bao, C. Yu and P. Pan, *Small*, 2023, **19**, 2205960.
- 3 R. Khalilzadeh, M. Babazadeh-Mamaqani, M. Mohammadi-Jorjafki, H. Roghani-Mamaqani and R. Hoogenboom, *Prog. Mater. Sci.*, 2025, **153**, 101487.
- 4 A. Abdollahi, H. Roghani-Mamaqani, B. Razavi and M. Salami-Kalajahi, *ACS Nano*, 2020, **14**, 14417–14492.



- 5 S. Liu, J. Wang, F. Tang, N. Wang, L. Li, C. Yao and L. Li, *ACS Appl. Mater. Interfaces*, 2020, **12**, 55269–55277.
- 6 V. Anand, R. Mishra and Y. Barot, *Dyes Pigm.*, 2021, **191**, 109390.
- 7 H. Wang, Y. Li, Y. Zhang, J. Mei and J. Su, *Chem. Commun.*, 2019, **55**, 1879–1882.
- 8 M. Hao, G. Sun, M. Zuo, Z. Xu, Y. Chen, X. Hu and L. Wang, *Angew. Chem., Int. Ed.*, 2020, **59**, 10095–10100.
- 9 H.-T. Feng, X. Zheng, X. Gu, M. Chen, J. W. Y. Lam, X. Huang and B. Z. Tang, *Chem. Mater.*, 2018, **30**, 1285–1290.
- 10 X.-Q. Chen, S.-C. Wang, M. An, Z. Chen and Z. Wang, *ACS Mater. Lett.*, 2025, **7**, 417–424.
- 11 N. Asadi-Zaki, H. Mardani, H. Roghani-Mamaqani and M. Salami-Kalajahi, *ACS Appl. Nano Mater.*, 2024, **7**, 14695–14706.
- 12 J. Tang, T. Xing, S. Chen and J. Feng, *Small*, 2024, **20**, 2305928.
- 13 C. Yang, H. Xiao, L. Tang, Z. Luo, Y. Luo, N. Zhou, E. Liang, G. Wang and J. Tang, *Mater. Horiz.*, 2023, **10**, 2496–2505.
- 14 W. Cheng, X. Wu, Y. Zhang, D. Wu, L. Meng, Y. Chen and X. Tang, *Trends Food Sci. Technol.*, 2022, **129**, 244–257.
- 15 T. Liu, R. Meng, X. Su and S. Wu, *J. Colloid Interface Sci.*, 2025, **684**, 531–539.
- 16 B. Kumari, R. Dahiwardkar and S. Kanvah, *Aggregate*, 2022, **3**, e191.
- 17 Y. Zuo, X. Wang and D. Wu, *J. Mater. Chem. C*, 2019, **7**, 14555–14562.
- 18 Y. Liang, J. Wei, J. Zhang, T. Zhang, C. Guo, Y. Li, X. Ma, M. Liu and Y. Yan, *J. Mater. Chem. C*, 2025, **13**, 4104–4111.
- 19 J. Wang, F. Tang, Y. Wang, S. Liu and L. Li, *Adv. Opt. Mater.*, 2020, **8**, 1901571.
- 20 T. Förster, *J. Biomed. Opt.*, 2012, **17**, 011002–011002.
- 21 M. Li, R. Wang, Y. Xia, Y. Fu, L. Wu, G. Sun, J. Zhu, Y. Tang and Y. Yao, *Macromol. Rapid Commun.*, 2025, **46**, 2400929.
- 22 T. Xiao, D. Ren, L. Tang, Z. Wu, Q. Wang, Z.-Y. Li and X.-Q. Sun, *J. Mater. Chem. A*, 2023, **11**, 18419–18425.
- 23 G. Zhang, L. Yu, J. Chen, R. Dong, N. Godbert, H. Li and J. Hao, *J. Phys. Chem. Lett.*, 2022, **13**, 8999–9006.
- 24 N. Asadi-Zaki, H. Mardani, H. Roghani-Mamaqani and F. Wang, *Coord. Chem. Rev.*, 2024, **500**, 215518.
- 25 X. Ma, Y. Liang, J. Wei, J. Zhang, E. Feng, Z. Fu, S. Lian and Y. Yan, *ACS Appl. Opt. Mater.*, 2024, **2**, 1903–1910.
- 26 H. Mardani, A. Herizchi and H. Roghani-Mamaqani, *Chem. Eng. J.*, 2024, **490**, 151751.
- 27 W. Humphrey, A. Dalke and K. Schulten, *J. Mol. Graphics*, 1996, **14**, 33–38.
- 28 T. Lu and F. Chen, *J. Comput. Chem.*, 2012, **33**, 580–592.
- 29 D. Aigner, B. Ungerböck, T. Mayr, R. Saf, I. Klimant and S. M. Borisov, *J. Mater. Chem. C*, 2013, **1**, 5685–5693.
- 30 Y. Zhang, B. Lei and X. Zhang, *Chem. Commun.*, 2022, **58**, 5261–5264.
- 31 Y. Wu, Y. Shi and H. Wang, *Macromolecules*, 2023, **56**, 4491–4502.

